

Photoemission and Injection Properties of a Vacuum Photodiode with Two Negative-Electron-Affinity Semiconductor Electrodes

A. A. Rodionov,¹ V. A. Golyashov,¹ I. B. Chistokhin,¹ A. S. Jaroshevich,¹ I. A. Derebezov,¹ V. A. Haisler,¹ T. S. Shamirzaev,^{1,2} I. I. Marakhovka,^{1,2} A. V. Kopotilov,³ N. V. Kislykh,³ A. V. Mironov,³ V. V. Aksenov,³ and O. E. Tereshchenko^{1,2}

¹*Rzhanov Institute of Semiconductor Physics SB RAS, 630090 Novosibirsk, Russian Federation*

²*Novosibirsk State University, 630090 Novosibirsk, Russian Federation*

³*CJSC "EKRAAN FEP", 630060 Novosibirsk, Russian Federation*

(Received 15 May 2017; revised manuscript received 15 August 2017; published 26 September 2017)

The photoemission and injection properties of two GaAs/(Al,Ga)As electrodes with effective negative electron affinity (NEA) are studied in the parallel-plate capacitorlike vacuum photodiode. Both electrodes are bonded to the glass of the input windows, allowing measuring the quantum yield in the transmission and reflection modes. The photodiode with NEA states of both electrodes is sensitive to the illumination in the 400–900 nm range and produces the photocurrent with no bias applied between electrodes. The energy distribution of emitted electrons is studied as a function of the transverse energy component to the surface in the temperature range of 20–300 K. The presence of the fine structure in the photoemission spectra is associated with the electron-phonon coupling in two-dimensional quantized states in the band-bending region. The two-electrode vacuum photoemission system demonstrates the negative differential conductivity. The cathodoluminescence signal is measured as a function of free-electron injection energy with the threshold appearance less than 0.05 V between electrodes.

DOI: [10.1103/PhysRevApplied.8.034026](https://doi.org/10.1103/PhysRevApplied.8.034026)

I. INTRODUCTION

Despite a relatively long (more than 50 years) history of photoemitters with effective negative electron affinity (NEA), there still remain a lot of unsolved questions in photoemission physics and in reaching the limiting parameters of devices based on various semiconductor photocathodes with NEA [1–3]. The *p*-GaAs(001)-(Cs, O) system with NEA is widely used to create ultrasensitive (photon-counting), low-noise, and high-speed photodetectors, as well as the sources of ultracold and the spin-polarized electrons [4–11]. Recently, it was also demonstrated that the vacuum systems with a low work function may also be prospective for solar-cell applications [12,13].

The process, inverse to emission, is the electron injection into the semiconductor structure [14]. Because of the time-reversal nature of Maxwell and Schrödinger equations, the injection of spin-polarized electrons into GaAs and their subsequent recombination create the polarized cathodoluminescence emission. Thus, vacuum photodiodes consisting of two semiconductor electrodes with NEA can be used to study the injection properties of low-energy electrons and to measure the spin polarization of free electrons [15–17]. This should allow modeling a new type of spin detectors for free electrons with spatial resolution. Such an injection type of spin detection based on the electron-photon conversion is alternative to the spin detection based on spin-orbital or exchange interactions [18–21].

The energy and angular distribution of emitted low-energy spin-polarized electrons into the vacuum from

p-GaAs(001)-(Cs, O) is still a subject of intensive investigations [22–24]. The vacuum photodiodes with one semiconductor electrode have already showed their capability in studying interesting photoemission physics and spin-dependent effects [25,26]. The vacuum photodiode with two NEA electrodes with a total volume of about 6 cm³ (vacuum volume less than 0.3 cm³) provides several advantages combining the possibilities of huge vacuum systems: The GaAs (or III–V superlattices) cathode can be used as a source of spin-polarized electrons [27,28]; the GaAs surface-preparation technology allows obtaining an atomically flat surface with a homogeneous potential over the macroscopic surface area that gives a possibility to study electron energy distribution with a high resolution; two NEA electrodes with equivalent work functions do not produce the contact potential difference (CPD), and, as a result, photoemitted electrons are not sensitive to the stray electric field (this effect is difficult to exclude in vacuum systems, in particular, in angular-resolved photoemission spectroscopy); the semiconductor anode can be used as a detector of spin-polarized electrons through the detection of the cathodoluminescence polarization from injected electrons [15]. All measurements with the photodiode mentioned above can be easily performed at cryogenic temperatures and in the magnetic field. The detailed study of the energy distribution of the photoemitted electrons, related to the electron-phonon coupling, spin-dependent injection, and detection of free electrons with spatial resolution and solar-cell properties of the

vacuum photodiode with NEA electrodes, will be published elsewhere.

In this work, the emission and injection processes are studied by the retarding field method [29] in the vacuum photodiode with two NEA semiconductor electrodes to demonstrate a wide possibility of the developed system.

II. EXPERIMENTAL DETAILS

The manufactured photodiode is an axially symmetric vacuum tube with semiconductor structures at the ends. The cross section of this vacuum photodiode is shown schematically in Fig. 1(a). The diameter of the electrodes is 20 mm, and the vacuum gap between them is about 1 mm. This planar vacuum photodiode consists of two identical NEA p -GaAs(001)-(Cs, O) mounted parallel on the edges of a cylindrical alumina ceramic body. The active 2.5- μ m-thick GaAs layer is passivated by the (Al,Ga)As layer for suppressing the illuminated surface recombination [30]. The structures are bonded to the glass by the (Al,Ga)As layer through the silicon monoxide (SiO) antireflection coating. The active-layer surface-cleaning procedure is performed inside a glovebox, flooded with pure nitrogen, where the structures are chemically treated in the solution of HCl in isopropanol [31]. Cleaned surfaces are activated to the NEA state by coadsorption of cesium and oxygen. Ultimately, both structures are sealed in vacuum parallel to each other on the opposite sides of the alumina ceramic cylinder.

In the created design of the vacuum photodiode, both electrodes can play the role of the cathode or anode, depending on the sign of the applied voltage, and work in transmission (t mode) or reflection (r mode) modes. Hereinafter, we designate them as electrode 1 (el_1) and electrode 2 (el_2). In the previous contributions on the study of electron photoemission in planar photodiodes, a metal is used as the anode material. Therefore, it is necessary to apply an additional voltage to compensate a contact potential difference of about 3 V [25,26]. Moreover, metals, being microstructured, can have a greater variation in the magnitude of the work function on the surface than single-crystal semiconductor electrodes. The main feature of the created vacuum photodiode is that both electrodes are semiconductor heterostructures with close work functions, and the vacuum levels of both electrodes are below the conduction-band minimum in the bulk, being in the so-called negative-electron-affinity state shown in the band diagram of two semiconductor electrodes (Fig. 2). This leads to the typical photocurrent-voltage characteristic (I - V curve) shown in Fig. 1(b). One can see that, at $V = 0$, the photocurrent flows in the vacuum diode, and the compensated photovoltage (open-circuit voltage) value is about 0.3 V.

Because of the photodiode axial symmetry, illumination can be performed on both sides of the electrodes, and that allows measuring both quantum yield [$QY(\lambda)$] spectra and photoelectron energy distributions $N(E_{\perp})$ using the photodiode as a retarding field electron spectrometer, which

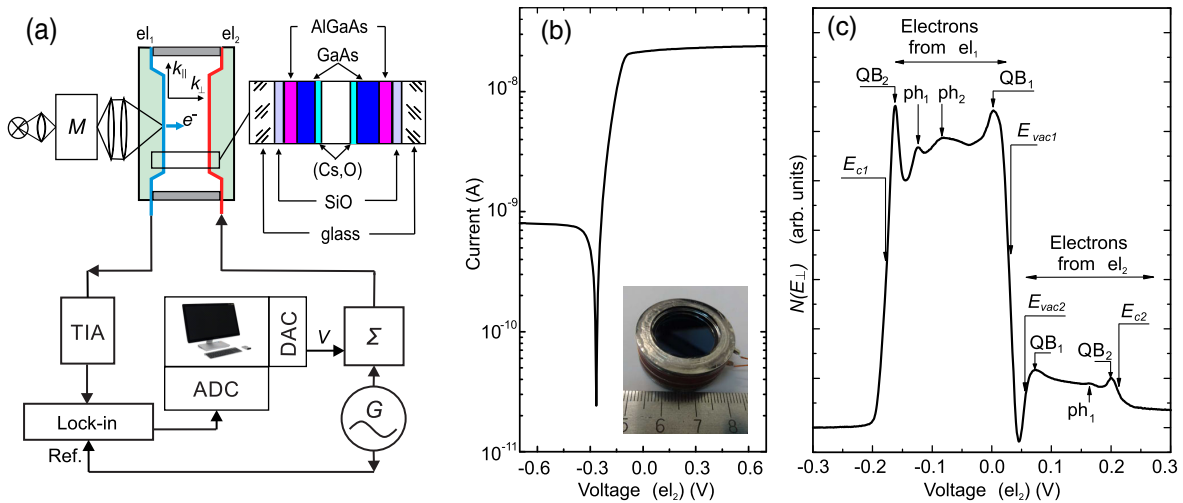


FIG. 1. (a) Schematic presentation of a compact vacuum photodiode for the investigation of electron emission and injection properties. The enlarged images of the cathode and anode structures bonded to glass, which consist of the antireflection SiO layer, (Al,Ga)As layer, p -GaAs active layer, and Cs-O activation layer, are shown in the inset. The measurement circuit consists of the halogen lamp, monochromator (M), vacuum photodiode, digital-analog converter (DAC), generator (G), amplitude adder (Σ), transimpedance amplifier (TIA), current-to-voltage converter, lock-in amplifier, analog-digital converter (ADC), and computer. (b) I - V curve for the 780-nm excitation at 300 K; the inset shows a photo of the vacuum photodiode. (c) Emitted electron energy distribution $N(E_{\perp})$ for the 780-nm excitation wavelength at 20 K. The energies corresponding to the vacuum level E_{vac} and to the conduction band E_c bottom are shown with the vertical arrows. The negative retarding voltage corresponds to the EDC from el_1 (cathode), while the positive from el_2 (anode). QB_i features reflect the emission from quantized levels, and ph_i losses on phonon scattering.

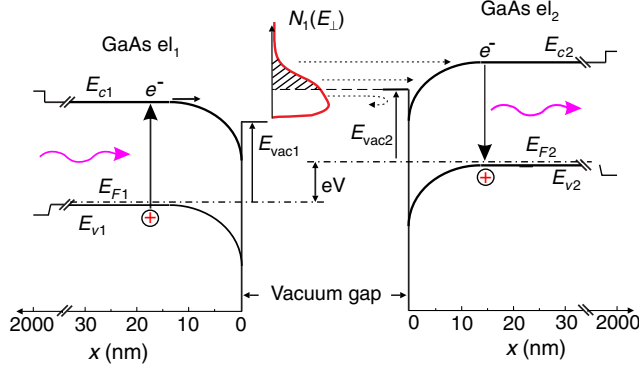


FIG. 2. Band diagram of the vacuum photodiode with two NEA semiconductor electrodes. E_c , conduction band; E_v , valence band; E_F , Fermi level; E_{vac} , vacuum level; V , bias between electrodes (el_2 has negative potential); $N_1(E_{\perp})$, energy distribution of electrons emitted from el_1 .

allows measuring the energy distribution on the transverse component (E_{\perp}). In the case where el_1 is illuminated, the photodiode works in the transmission mode (t mode) for el_1 absorbing the major part of the incident light in el_1 . A small amount of incident light can reach el_2 , passing through el_1 , and cause the photoemission from el_2 . In this case, el_2 works in the reflection mode (r mode). The band diagram of the photodiode with the applied retarding field for the electrons emitted from el_1 is demonstrated in Fig. 2. The electrons photoemitted from el_1 are partly held by the applied field. At the same time, electrons emitted from el_2 are accelerated by this field. Thus, in the two-photocathode system, photoemitted electrons have some energy distributions $N_1(E_{\perp})$ (from el_1) and $N_2(E_{\perp})$ (from el_2 , not shown in Fig. 2).

The retarding field cuts off the low-energy electrons, and only electrons with energies higher than the potential barrier are detected. The measured current in the retarding field analyzer in the general case is given by

$$I(V) = \int_{V^*}^{\infty} eN(U)dU, \quad (1)$$

where $V^* = V + V_{CPD}$, V is a retarding potential, and V_{CPD} —contact potential difference between electrodes, which is, in our case, close to zero $V_{CPD} \approx 0$; $eN(U)dU$ —is the current caused by the electrons with the energy in the range from eU to $e(U + dU)$. In the case of the photodiode with two NEA electrodes, not only direct (from a cathode) but also inverse (from an anode) current should be taken into account due to the light absorption in the anode (r mode for an anode). Then, with an applied voltage V at el_2 and grounded el_1 , the total current can be represented as

$$J(V) = \int_{E_{vac2}-eV}^{\infty} eN_1(E_{\perp})dE_{\perp} - \int_{E_{vac1}}^{\infty} eN_2(E_{\perp} + eV)dE_{\perp}, \quad (2)$$

where $N_i(E_{\perp})$ is the distribution over the energies on the transverse motion of the electrons emitted from an i th electrode; E_{vac_i} is the vacuum level of an i th electrode. The first term corresponds to the el_1 contribution to the total current, and the second to the el_2 . It is expected that electrons with energies above the vacuum level are free to enter the corresponding electrode and those with lower energies reflect backward from the potential barrier. The derivative $d(J/e)/d(eV) = N(E_{\perp})$ is the electron transfer energy distribution in the emitted current. Differentiating the retarding curve Eq. (2), we get

$$\frac{dJ}{dV} \propto N_1(E_{vac2} - eV) + N_2(E_{vac1} + eV). \quad (3)$$

In a general case, we measure the sum of the first and second electrode distributions. However, first, the second term in Eq. (3) is smaller due to the light absorption in the illuminated electrode. Second, to measure $N_1(E_{\perp})$, we need to gradually increase the barrier V while, for $N_2(E_{\perp})$, this is an accelerating potential, and a change in V does not affect the second term in Eq. (3), since the derivative is zero. Accordingly, at $V < 0$ (with the accuracy to CPD), we measure the $N_1(E_{\perp})$ distribution of el_1 , while at $V > 0 - N_2(E_{\perp})$, it is the emitted electron energy distribution from el_2 .

To measure the energy distribution curve (EDC) of emitted electrons, it is necessary to differentiate the delay curve [Eq. (2)] that can be done mathematically or experimentally. To avoid additional errors induced by mathematical derivation, the EDCs are measured by differentiating delay curves using the lock-in technique. The experimental scheme for measuring the EDC based on the retarding field analyzer is shown in Fig. 1(a). The vacuum photodiode is illuminated by light produced by the halogen lamp and monochromator. The illuminated electrode acts as a photocathode and is virtually grounded via the transimpedance amplifier (TIA). A sine wave with the pk - pk amplitude $\delta V = 5$ mV and frequency 165 Hz is added to bias voltage V , and the total signal is applied to the opposite electrode. The TIA output signal [Eq. (3)], proportional to EDC, is measured using the lock-in technique. A typical EDC at 20 K is shown in Fig. 1(c). The energy resolution of our measurements is evaluated as the steepest slopes of EDC and amount to 10 meV at $T = 20$ K, 14 meV at $T = 100$ K, and 28 meV at $T = 300$ K.

The design of our vacuum diode also allows studying the process of free-electron injection into NEA GaAs. It is obvious that electrons injected into the p -GaAs will recombine with holes, producing the cathodoluminescence (CL). In order to measure it, the bias voltage is modulated with the unipolar square wave of amplitude $\delta V = 5$ mV and frequency 33 Hz. The CL signal at the corresponding frequency is measured through the monochromator-based optical system using the silicon photodiode as a detector and a lock-in amplifier.

III. RESULTS AND DISCUSSION

A. Photoemission properties: Quantum yield and electron energy distribution measurements

The QY spectra measured in the t mode for both electrodes without any voltage applied between electrodes are shown in Fig. 3(a). The quantum yield is calculated as the ratio of the registered electrons per incident photons. The QY spectra of both electrodes are typical of photoemitters with NEA GaAs(Cs,O) [32] and well coincide with each other. The quantum yield is almost constant in the range of 575–880 nm with a maximum of about 17% at the zero applied voltage. The photoemission threshold of QY spectra is determined by the energy gap of GaAs (1.42 eV/880 nm), while the QY reduction at $\lambda < 560$ is caused by the increase of light absorption in the (Al,Ga)As layer, and it decreases down to about 0.4% at 400 nm. Thus, even without an additional applied voltage, photoemitted

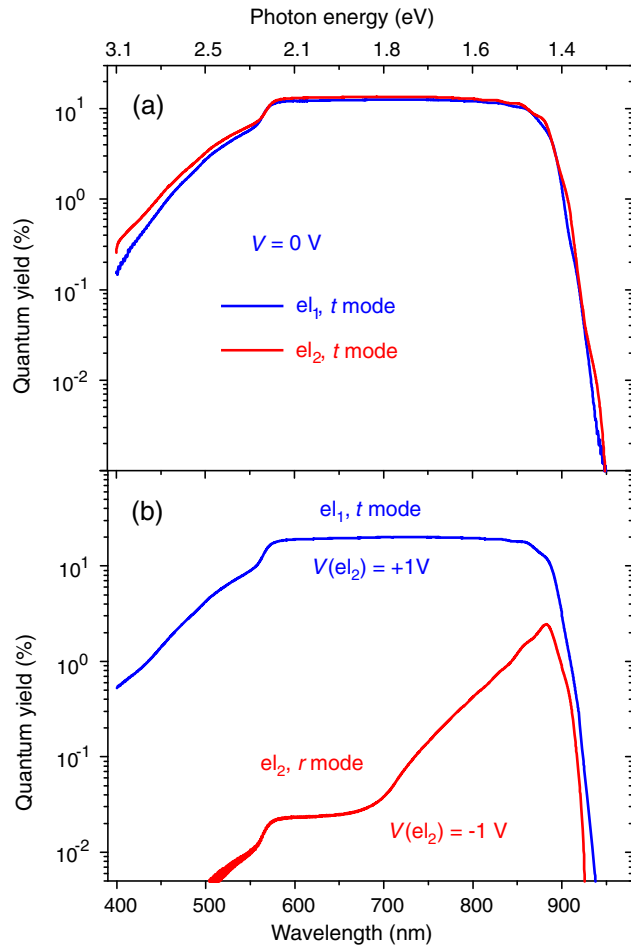


FIG. 3. (a) Quantum yield as a function of the incident photon wavelength measured in the t mode for both electrodes at $V = 0$ V between electrodes. (b) QY of el_1 in the t mode at $V(el_2) = +1$ V (blue curve), and QY of el_2 in the r mode at $V(el_2) = -1$ V (red curve); $T = 300$ K.

electrons are able to reach a counterelectrode in a wide wavelength range (400–900 nm), and it produces a current. This gives an idea that a photodiode with two NEA semiconductor electrodes can be used as the solar-energy converter based on a photoemission solar cell. The spectral power-conversion efficiency of the GaAs-GaAs photodiode is only about 1%. However, we would like to stress that both electrodes are p -type GaAs with the equal position of the Fermi level in the bulk and at the surface.

The QY spectra with the applied bias between electrodes under the illumination of el_1 are shown in Fig. 3(b). In the case of $V(el_2) = +1$ V, we register the electrons from el_1 working in the t mode. In the transmission mode, the additional voltage increases QY from 17% to 23% due to the reduction of the space-charge effect and reverse current [second terms in Eqs. (2) and (3)]. In the case of $V(el_2) = -1$ V, the electrons emitted from el_2 are detected at el_1 (el_2 works in the r mode). The discrepancy in QY in the reflection and transmission modes is caused by the light absorption in the illuminated el_1 electrode. QY in the r mode reaches its maximum of 2.5% at $\lambda = 883$ nm.

To study the electron emission process via the electron energy distribution, the photoelectron spectra (energy distribution curves) are measured by differentiating the delay curves using the lock-in technique [Fig. 1(a)]. The EDC under the illumination of el_1 for different wavelengths are shown in Fig. 4. The bottom axis corresponds to the voltage at el_2 ; thereby, at the negative voltage, the photoelectrons emitted from el_1 are in the retarding electric field, and the corresponding EDC $N_1(E_\perp)$ is registered. At the positive voltage, most of the electrons emitted from el_1 are collected, and only the electrons photoemitted or/and reflected from el_2 , being in the retarding electric field, are registered [$N_2(E_\perp)$]. The shape of EDC from el_1 is independent from the wavelength, and that can be explained by the fact that el_1 works in the t mode and all electrons, regardless of the wavelength, are thermalized, because the cathode thickness ($2.5 \mu\text{m}$) exceeds the light absorption length ($\lesssim 1.0 \mu\text{m}$). The maximum (thermalized) electron energy is determined by the highest negative retarding voltage, and it corresponds to the energy of the electrons emitted from the conduction band, indicated as E_{c1} in Figs. 1(c) and 4 and explained by the band diagram in Fig. 2. The electrons with the lowest energies are emitted from the el_1 vacuum level indicated as $E_{\text{vac}1}$. The positions of the vacuum level and the bottom of the conduction band in EDC are determined as the inflection points at the edges of distributions, and its difference gives a value of NEA χ^* .

In contrast to el_1 , part of the EDC, distributed mostly from el_2 , depends on the wavelength. Note that el_2 works in the r mode for the EDC shown in Fig. 4. The intensity and shape of the $N_2(E_\perp)$ distribution change in the range of 800–900 nm, and they are very weakly dependent on the wavelengths below 800 nm. The EDC, measured as a function of the wavelength, demonstrates that, with the

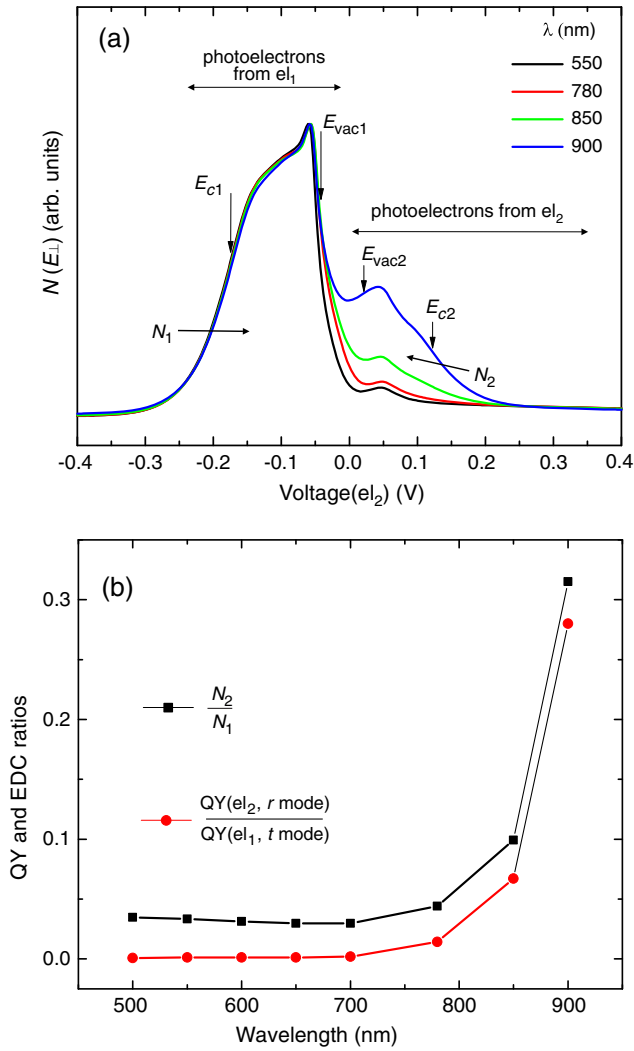


FIG. 4. (a) Normalized energy distribution curves of the photodiode under the illumination of el_1 for different excitation wavelengths ($T = 300$ K). (b) The ratio of N_2 integral intensity to that of N_1 (black squares) and $QY(r \text{ mode})/QY(t \text{ mode})$ (red circles), as taken from Fig. 3(b).

increase of the wavelength, the fraction of electrons from el_2 increases. The number of electrons detected from el_1 and el_2 (N_1 and N_2 , respectively) corresponds to the area under EDC curves for negative and positive retarding voltages, respectively, which are proportional to the QY of the respective electrode.

The ratio N_2/N_1 should follow the ratio of QYs, shown in Fig. 4(b). However, the N_2/N_1 ratio exceeds the ratio of the corresponding QYs over the entire wavelength range, and that indicates the presence of an additional contribution to the measured EDC, which cannot be explained only by the photoemission from el_2 . We connect this discrepancy with the presence of reemitted electrons, which were photoemitted from el_1 and reemitted by el_2 with a loss of energy or electrons that are reflected by the electric field in the gap and return to el_1 (cathode) with the energy above

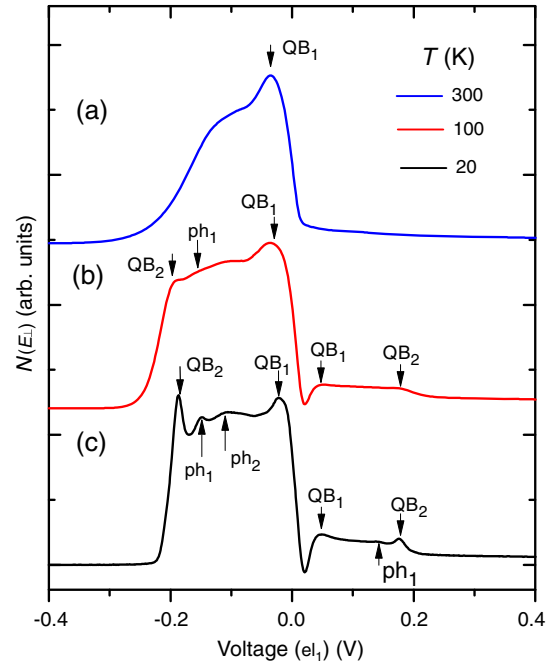


FIG. 5. Normalized EDC under the illumination of el_2 with the 780-nm wavelength at (a) 300, (b) 100, and (c) 20 K. The spectra measured at low temperature are shifted to the position of peak QB_1 at 300 K. Negative voltage values correspond to the electron photoemitted from el_2 , positive values to that photoemitted from el_1 .

the cathode vacuum level. These electrons first occupy the conduction band from which they can be again reemitted. The ratio of N_2 integral intensity to that of N_1 is $N_2/N_1 = 0.04$ in the whole wavelength range. Thus, we can conclude that, for low-energy electrons (0–300 meV), the reemission coefficient from the (Cs,O)-covered GaAs(001) surface is less than 5%.

The emitted electron energy distribution provides important information about the electron energy loss mechanism during the emission. The distribution curves of emitted electrons $N(E_{\perp})$ in the transmission mode for the 780-nm excitation wavelength measured at 300, 100, and 20 K are shown in Figs. 5(a)–5(c). Note that the horizontal axis represents the voltage applied to the cathode or anode (directly related to the electron energy), where it is seen that, at zero potential, the photocurrent flows in a wide spectral range. It is also seen that both the cathode and anode contribute to the EDC.

The temperature reduction of the emitter is known to reduce the temperature broadening, and it allows elucidating the microscopic scattering mechanisms. The electron energy distribution measured for the p^+ -GaAs(Cs,O) transmission-mode photocathode at 20 K is presented in Fig. 5(c). At 20 K, we can observe the most complete list of features that are marked as QB_1 – QB_2 and ph_1 – ph_2 for both electrodes. The QB_1 and QB_2 peaks are located 20 ± 5 and 180 ± 10 meV, respectively, below the bottom of the

conduction band in the semiconductor bulk and correspond to the electron emission from the quantized conduction-band subbands. The shape of the QB_2 peak in the vicinity of its maximum is well described by the Gaussian profile with the half-width of 30 meV. The small effective electron mass in the Γ valley ($(m^*/m) = \frac{1}{15}$) of GaAs, along with the conservation of longitudinal momentum at the surface, should cause the mean longitudinal energy to be lower than $(m^*/m)30 \text{ meV} = 2 \text{ meV}$ and, as a result, a very narrow emission cone [33]. The separation of emitted electrons from the quantized QB_1 level by cutting low-energy electrons with the retarding potential gives an idea for a reduction in the mean longitudinal energy and, as a result, in the low emittance that is important for light-source applications and should allow the generation of short electron bunches from photoinjectors with superior beam brightness. Note that, in the photoemission from photocathodes with NEA, it is accepted that energy and momentum components along a surface are called transverse, and, for this reason, the mean transverse energy is considered [34,35].

Features ph_1 and ph_2 are observed on the low-energy side of the QB_2 peak. The energy gaps QB_2 - ph_1 and ph_1 - ph_2 between the features turned out to be approximately the same and equal to $38 \pm 1 \text{ meV}$, in agreement with earlier findings [25]. This value exceeds the energy of the long-wavelength longitudinal optical phonons $\hbar\omega(\text{LO}) = 36.7 \text{ meV}$ in GaAs and the energy of Fuchs-Kliewer surface phonons $\hbar\omega_{\text{FK}} = \hbar\omega_{\text{TO}}[(\epsilon_0 + 1)/(\epsilon_\infty + 1)]^{1/2}$, where $\hbar\omega_{\text{TO}} = 33.1 \text{ meV}$ —transverse optical phonon energy at the Γ point in the bulk—and ϵ_0 , and ϵ_∞ are the static and optical dielectric constants, respectively. For GaAs(001), the energy of Fuchs-Kliewer surface phonons is $\hbar\omega_{\text{FK}} = 36.2 \text{ meV}$ [36]. Peak QB_2 corresponds to the elastic and peaks ph_1 and ph_2 correspond to the inelastic electron emission from the upper QB_2 subband of a two-dimensional quantization band in the near-surface potential in the vacuum with the emission of one and two phonons, respectively. A more detailed analysis of the emission mechanism from the semiconductor photocathodes with NEA will be published elsewhere.

Besides the fine structure in EDC, the negative differential conductivity in the region of zero potential appears at a temperature below 130 K. To our knowledge, negative differential conductivity (NDC) has never been observed in a vacuum two-electrode system at almost a zero electric field. The total current reduction can be caused either by decreasing the first term in Eq. (2) or by increasing the second one. Taking into account the fact that the second term is almost 2 orders of magnitude smaller than the first one (Fig. 3), it is reasonable to assume that the NDC is caused by the decrease of the direct photocathode current. Reducing the direct current at a low accelerating potential can be caused by the effect of the interference of photoemitted low-energy electrons on the surface potential

induced by the image potential and electrostatic field. The explanation of the observed NDC should involve the calculation of field-dependent transmission coefficients for electrons escaping over the mirror-image-applied electrostatic field potential barrier at the emitting surface. A further study is needed to describe the NDC mechanism in a two-electrode system more accurately.

B. Low-energy electron injection in p -GaAs(Cs,O): Cathodoluminescence study

The CL (cathodoluminescence) spectrum versus wavelength measured at 2 V and PL (photoluminescence) spectra from the same electrode e_2 are shown in Fig. 6(a). The cathodoluminescence intensity at 880 nm, as a function of the applied modulated bias at e_2 (equal to the energy of the injected electrons) together with the I - V curve, is shown in Fig. 6(b).

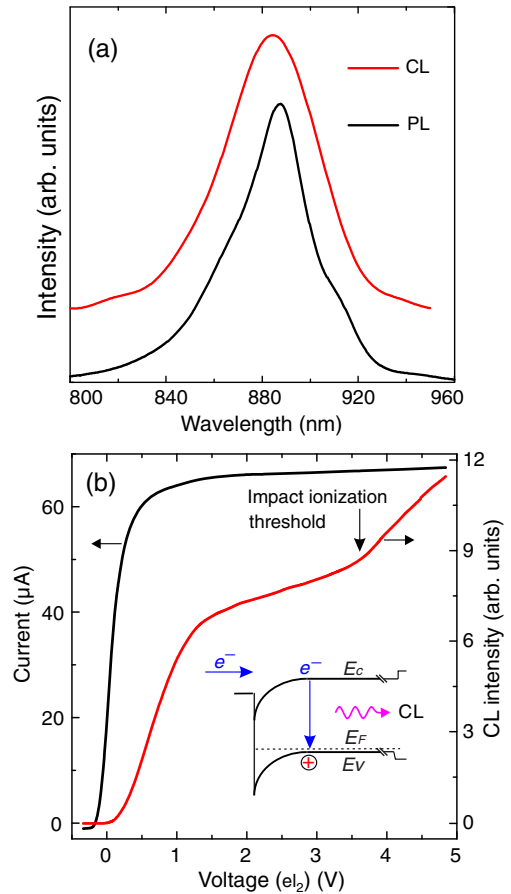


FIG. 6. (a) Cathodoluminescence (red curve) and photoluminescence (black curve) spectra from the e_2 ; the CL spectrum is measured at 2 V between the electrodes. (b) Photocurrent (black curve) and cathodoluminescence intensity (red curve) as a function of applied bias at e_2 . The inset shows a scheme of electron injection in the anode (e_2) and radiative recombination of this electron with cathodoluminescence emission.

The CL signal starts to rise around 0 V when the modulation voltage is applied. One can see that the photocurrent is close to saturation at 0.5–1.0 V, while the CL signal continues to increase with the electron energy. The intensity rapidly increases starting from 0 to 1 V, caused by the electron injection into the semiconductor bulk and their subsequent radiative recombination. When the voltage increases to 1 V, the major part of the electrons get into the anode bulk and the intensity growth slows down. There is a subsequent rise in the CL curve above 3.6 eV, which coincides with the onset of electron-hole pair creation by impact ionization [37], while the current remains constant. During this process, the primary electron excites an additional secondary electron into the conduction band. Then both electrons recombine with the emission of two photons. A study of spin-dependent injection and the detection of free electrons with spatial resolution is in progress.

IV. CONCLUSION

In summary, we study the photoemission and injection properties of the vacuum photodiode with two negative-electron-affinity semiconductor electrodes. The equivalence of both single-crystal semiconductor electrodes allows excluding the CPD between electrodes and the work function inhomogeneity inherent for metal electrodes. The NEA states of both electrodes allow measuring the photocurrent in the 400–900 nm range with no bias applied between electrodes with an energy-conversion efficiency about 1%, and that gives an idea for the further development of a two-NEA-electrode system for the application in solar-energy conversion. The energy distribution of emitted electrons is studied as a function of the transverse energy component in the 20–300 K temperature range. The presence of the fine structure in the photoemission spectra, associated with the electron-phonon coupling in two-dimensional quantized states in the band-bending region, is demonstrated. The cathodoluminescence signal is measured as a function of the electron injection energy with the threshold appearance less than 0.05 V between electrodes.

ACKNOWLEDGMENTS

This study is supported by the Russian Science Foundation (Project No. 17-12-01047).

-
- [1] R. L. Bell, *Negative Electron Affinity Devices* (Oxford University, New York, 1973).
 - [2] Y. Zhang, J. Niu, J. Zhao, J. Zou, B. Chang, F. Shi, and H. Cheng, Influence of exponential-doping structure on photoemission capability of transmission-mode GaAs photocathodes, *J. Appl. Phys.* **108**, 093108 (2010).
 - [3] K. Sahasrabudde, J. W. Schwede, I. Bargatin, J. Jean, R. T. Howe, Z.-X. Shen, and N. A. Melosh, A model for emission

- yield from planar photocathodes based on photon-enhanced thermionic emission or negative-electron-affinity photoemission, *J. Appl. Phys.* **112**, 094907 (2012).
- [4] R. A. La Rue, K. A. Costello, C. Davis, J. P. Edgecumbe, and V. W. Aebi, Photon counting III-V hybrid photomultipliers using transmission mode photocathodes, *IEEE Trans. Electron Devices* **44**, 672 (1997).
- [5] D. Orlov, U. Weigel, D. Schwalm, A. Terekhov, and A. Wolf, Ultra-cold electron source with a GaAs-photocathode, *Nucl. Instrum. Methods Phys. Res., Sect. A* **532**, 418 (2004).
- [6] D. Pierce, R. Celotta, G.-C. Wang, W. Unertl, A. Galejs, C. Kuyatt, and S. Mielczarek, The GaAs spin polarized electron source, *Rev. Sci. Instrum.* **51**, 478 (1980).
- [7] I. Bazarov, L. Cultrera, A. Bartnik, B. Dunham, S. Karkare, Y. Li, X. Liu, J. Maxson, and W. Roussel, Thermal emittance measurements of a cesium potassium antimonide photocathode, *Appl. Phys. Lett.* **98**, 224101 (2011).
- [8] N. B. Clayburn, J. L. McCarter, J. M. Dreiling, M. Poelker, D. M. Ryan, and T. J. Gay, Search for spin-polarized photoemission from GaAs using light with orbital angular momentum, *Phys. Rev. B* **87**, 035204 (2013).
- [9] X. Jin, A. Mano, F. Ichihashi, N. Yamamoto, and Y. Takeda, High-performance spin-polarized photocathodes using a GaAs/GaAsP strain-compensated superlattice, *Appl. Phys. Express* **6**, 015801 (2013).
- [10] N. Yamamoto *et al.*, Thermal emittance measurements for electron beams produced from bulk and superlattice negative electron affinity photocathodes, *J. Appl. Phys.* **102**, 024904 (2007).
- [11] T. Maruyama, A. Brachmann, J. Clendenin, T. Desikan, E. Garwin, R. Kirby, D.-A. Luh, J. Turner, and R. Prepost, A very high charge, high polarization gradient-doped strained GaAs photocathode, *Nucl. Instrum. Methods Phys. Res., Sect. A* **492**, 199 (2002).
- [12] J. W. Schwede *et al.*, Photon-enhanced thermionic emission for solar concentrator systems, *Nat. Mater.* **9**, 762 (2010).
- [13] J. Schwede *et al.*, Photon-enhanced thermionic emission from heterostructures with low interface recombination, *Nat. Commun.* **4**, 1576 (2013).
- [14] F.-J. Himpsel, Inverse photoemission from semiconductors, *Surf. Sci. Rep.* **12**, 3 (1990).
- [15] X. Li, O. E. Tereshchenko, S. Majee, G. Lampel, Y. Lassailly, D. Paget, and J. Peretti, Optical detection of spin-filter effect for electron spin polarimetry, *Appl. Phys. Lett.* **105**, 052402 (2014).
- [16] O. E. Tereshchenko, D. Lamine, G. Lampel, Y. Lassailly, X. Li, D. Paget, and J. Peretti, Transport and magnetic properties of Fe/GaAs schottky junctions for spin polarimetry applications, *J. Appl. Phys.* **109**, 113708 (2011).
- [17] O. E. Tereshchenko *et al.*, Ferromagnetic HfO₂/Si/GaAs interface for spin-polarimetry applications, *Appl. Phys. Lett.* **107**, 123506 (2015).
- [18] V. N. Strocov, V. N. Petrov, and J. Hugo Dil, Concept of a multichannel spin-resolving electron analyzer based on mott scattering, *J. Synchrotron Radiat.* **22**, 708 (2015).
- [19] F. Ji, T. Shi, M. Ye, W. Wan, Z. Liu, J. Wang, T. Xu, and S. Qiao, Multichannel Exchange-Scattering Spin Polarimetry, *Phys. Rev. Lett.* **116**, 177601 (2016).
- [20] C. Thiede, C. Langenkämper, K. Shirai, A. B. Schmidt, T. Okuda, and M. Donath, Reflectivity and Sherman Maps of

- Passivated Fe(001): Working Points for a Display-Type Spin-Polarization Analyzer, *Phys. Rev. Applied* **1**, 054003 (2014).
- [21] C. Tusche, M. Ellguth, A. Krasnyuk, A. Winkelmann, D. Kutnyakhov, P. Lushchyk, K. Medjanik, G. Schönhense, and J. Kirschner, Quantitative spin polarization analysis in photoelectron emission microscopy with an imaging spin filter, *Ultramicroscopy* **130**, 70 (2013).
- [22] N. Yamamoto *et al.*, High brightness and high polarization electron source using transmission photocathode with GaAs-GaAsP superlattice layers, *J. Appl. Phys.* **103**, 064905 (2008).
- [23] S. Karkare, D. Dimitrov, W. Schaff, L. Cultrera, A. Bartnik, X. Liu, E. Sawyer, T. Esposito, and I. Bazarov, Monte Carlo charge transport and photoemission from negative electron affinity GaAs photocathodes, *J. Appl. Phys.* **113**, 104904 (2013).
- [24] D.-I. Lee, Y. Sun, Z. Liu, S. Sun, and P. Pianetta, Angular dependence of the photoelectron energy distribution of InP(100) and GaAs(100) negative electron affinity photocathodes, *Appl. Phys. Lett.* **91**, 192101 (2007).
- [25] A. S. Terekhov and D. A. Orlov, Fine structure in the spectra of thermalized photoelectrons emitted from GaAs with a negative electron affinity, *JETP Lett.* **59**, 864 (1994).
- [26] D. A. Orlov, V. L. Alperovich, and A. S. Terekhov, Magnetically induced spin-dependent photoemission from p-GaAs (Cs,O) into vacuum, *Phys. Rev. B* **77**, 205325 (2008).
- [27] T. Maruyama, R. Prepost, E. Garwin, C. K. Sinclair, B. Dunham, and S. Kalem, Enhanced electron spin polarization in photoemission from thin GaAs, *Appl. Phys. Lett.* **55**, 1686 (1989).
- [28] T. Nakanishi, K. Dohmae, S. Fukui, Y. Hayashi, I. Hirose, N. Horikawa, T. Ikoma, Y. Kamiya, M. Kurashina, and S. Okumi, Construction of GaAs spin-polarized electron source and measurements of electron polarization, *Jpn. J. Appl. Phys.* **25**, 766 (1986).
- [29] J. A. Simpson, Design of retarding field energy analyzers, *Rev. Sci. Instrum.* **32**, 1283 (1961).
- [30] J. Zou, Y. Zhang, W. Deng, J. Jin, and B. Chang, Effect of different epitaxial structures on GaAs photoemission, *Appl. Opt.* **50**, 5228 (2011).
- [31] O. E. Tereshchenko, S. I. Chikichev, and A. S. Terekhov, Composition and structure of HCl-isopropanol treated and vacuum annealed GaAs(100) surfaces, *J. Vac. Sci. Technol. A* **17**, 2655 (1999).
- [32] D. Fisher, R. Enstrom, J. Escher, H. Gossenberger, and J. Appert, Photoemission characteristics of transmission-mode negative electron affinity GaAs and (In,Ga) as vapor-grown structures, *IEEE Trans. Electron Devices* **21**, 641 (1974).
- [33] Z. Liu, Y. Sun, P. Pianetta, and R. Pease, Narrow cone emission from negative electron affinity photocathodes, *J. Vac. Sci. Technol. B* **23**, 2758 (2005).
- [34] S. Karkare and I. Bazarov, Effect of nanoscale surface roughness on transverse energy spread from GaAs photocathodes, *Appl. Phys. Lett.* **98**, 094104 (2011).
- [35] S. Karkare and I. Bazarov, Effects of Surface Nonuniformities on the Mean Transverse Energy from Photocathodes, *Phys. Rev. Applied* **4**, 024015 (2015).
- [36] W. Mönch, *Semiconductor Surfaces and Interfaces* (Springer Science, New York, 2013), Vol. 26.
- [37] V. L. Alperovich, A. S. Terekhov, A. S. Jaroshevich, G. Lampel, Y. Lassailly, J. Peretti, N. Rougemaille, and T. Wirth, Polarized cathodoluminescence induced by low-energy spin-polarized electrons injected in p-GaAs(Cs, O), *Nucl. Instrum. Methods Phys. Res., Sect. A* **536**, 302 (2005).